MNRAS 000, 1–?? (2015) Preprint 1 March 2016 Compiled using MNRAS LATEX style file v3.0

Effects of Galactic Disc Inclination and Resolution on Observed GMC Properties and Larson's Scaling Relations

Hsi-An Pan[1], Yusuke Fujimoto[1], Elizabeth J. Tasker[1], Erik Rosolowsky[2], Dario Colombo[2,3], Samantha M. Benincasa[4], and James Wadsley[4]
[1] *Department of Physics, Faculty of Science, Hokkaido University, Kita 10 Nishi 8 Kita-ku, Sapporo 060-0810, Japan*
[2] *Department of Physics, 4-181 CCIS, University of Alberta, Edmonton, AB T6G 2E1, Canada*
[3] *Max Planck Institut für Radioastronomie, Auf dem Hügel 69, D-53121, Bonn, Germany*
[4] *Department of Physics and Astronomy, McMaster University, Hamilton, ON, L8S 4M1, Canada*

arXiv:1602.08670v1 [astro-ph.GA] 28 Feb 2016

Accepted XXX. Received YYY; in original form ZZZ

ABSTRACT

With ALMA making it possible to resolve giant molecular clouds (GMCs) in other galaxies, it is becoming necessary to quantify the observational bias on measured GMC properties. Using a hydrodynamical simulation of a barred spiral galaxy, we compared the physical properties of GMCs formed in position-position-position space (PPP) to the observational position-position-velocity space (PPV). We assessed the effect of disc inclination: face-on (PPV_{face}) and edge-on (PPV_{edge}), and resolution: 1.5 pc versus 24 pc, on GMC properties and the further implications of using Larson's scaling relations for mass-radius and velocity dispersion-radius. The low-resolution PPV data are generated by simulating ALMA Cycle 3 observations using the CASA package. Results show that the median properties do not differ strongly between PPP and PPV_{face} under both resolutions, but PPV_{edge} clouds deviate from these two. The differences become magnified when switching to the lower, but more realistic resolution. The discrepancy can lead to opposite results for the virial parameter's measure of gravitational binding, and therefore the dynamical state of the clouds. The power-law indices for the two Larson's scaling relations decrease going from PPP, PPV_{edge} to PPV_{face} and decrease from high to low resolutions. We conclude that the relations are not entirely driven by the underlying physical origin and therefore have to be used with caution when considering the environmental dependence, dynamical state, and the extragalactic CO-to-H_2 conversion factor of GMCs.

Key words: methods: numerical. – techniques: image processing. – galaxies: ISM. – ISM: clouds. – ISM: structure.

1 INTRODUCTION

As many observations show that star formation efficiency varies by ~ 100 times from galaxy to galaxy, increasing attention has been devoted to the questions of whether giant molecular cloud (GMC) properties are universal and whether their star formation ability depends on the large-scale galactic environment. The Atacama Large Millimeter/submillimeter Array (ALMA) observations are starting to resolve a wide population of GMCs with the quality of that in the Milky Way. This gives a chance to reveal the whole picture of the relation between GMCs and star formation in various environments. To interpret the measured GMC properties properly, it is necessary to understand any observational bias on the GMC properties.

It is still debated if the physical properties of continuous structure in the interstellar medium (ISM) measured by spectral line observations (e.g., ^{12}CO, HCN) represent the intrinsic structures in three-dimensions (e.g., Adler & Roberts 1992; Pichardo et al. 2000; Ostriker et al. 2001; Sheth et al. 2008; Shetty et al. 2010; Ward et al. 2012; Beaumont et al. 2013; Pan et al. 2015). Observations take data from the galaxies projected on the sky plane. This provides two spatial dimensions (RA and Dec.) and a velocity along the line of sight (LOS), known as the spectral data cube in Position-Position-Velocity space (PPV). However, the non-spherical shapes of GMCs change their appearances when projected along different LOS, which are determined by the inclination and position angle of the host galactic disc. Moreover, galaxies are distributed over a wide range in distance in the Universe, causing the physical resolution of observations to not always be the same. Finite resolution will necessarily introduce contributions from separated adjacent structures to the measured GMC properties.

© 2015 The Authors

These effects are assessable by comparing GMC properties in observations to simulations. Simulations normally have data with three-dimensional position (x, y, z) and velocity (v_x, v_y, v_z) coordinates, so called Position-Position-Position space (PPP), from which GMC properties can be directly calculated. In previous work, we compared the physical properties of the GMCs identified in PPP and those in PPV in the same simulated galaxy, assuming ideal circumstances, i.e., face-on observation with high resolution (1.5 pc) and sensitivity (1 K per 1 km s^{-1}) (Pan et al. 2015). The results show that PPP and PPV can potentially identify the same objects with closely matched properties within a scattering in value of a factor of 2. Yet such high resolution and sensitivity are very difficult to achieve in extragalactic observations even with ALMA.

In this work, we further evaluate the effects of galactic disc inclination and observed resolution. As in Pan et al. (2015), this is done by comparing GMCs in PPP and PPV. This paper is organized as follows. Method and datasets are introduced in Section 2. The cloud identification methods and the derivation of physical properties are introduced in Section 3. Section 4 presents the results of this work. We summarize the key results of our analysis in Section 5.

2 METHOD AND DATASETS

The simulated galaxies were modelled on the barred spiral (SABc) galaxy, M83, using observational data from the 2MASS K-band image to estimate the stellar potential. The simulations were run using the three dimensional adaptive mesh refinement (AMR) hydrodynamics code, ENZO (Bryan et al. 2014). The high-resolution (1.5 pc) simulation is presented in Fujimoto et al. (2014), along with a full description of the run parameters. The gas radiatively cooled down to 300 K but no star formation or feedback was included. Typical temperatures in the GMCs are about 10 K, an order of magnitude below our minimum radiative cooling temperature. However, our resolution is not sufficient to resolve the full turbulent structure of the gas and we also do not include pressure from magnetic fields. Including a temperature floor of 300 K therefore imposes a minimum sound speed of 1.8 km s^{-1} on the gas to crudely allow for these effects. The velocity dispersion within our GMCs is typically higher than this by about a factor of 2 – 3, implying that this floor does not have a significant impact on the cloud properties. Previous work that has compared runs with and without star formation and feedback physics suggest that GMC properties are not strongly affected by these additions. We have therefore not included a star formation model in this work, focusing on the properties of the gas (Tasker & Tan 2009; Tasker 2011; Tasker et al. 2015).

Face-on and edge-on projection images of the high-resolution simulated galaxy are shown in the bottom and top panels of Figure 2a. To assess the resolution effect, a low-resolution (24 pc) simulation was made by decreasing the total levels of refinement. The remaining run parameters are the same as in the high-resolution simulation.

There are six datasets in total, summarized in Table 1. Data structure of PPP, edge-on observation in PPV, and face-on observation in PPV are prepared. Each dataset is produced at two resolutions: 1.5 pc (with 1 km s^{-1} for PPV velocity axis) and ~ 24 pc (with 2 km s^{-1}). The high- and low-resolution PPP data using the aforementioned two simulations are presented as PPP$^{\rm H}$ and PPP$^{\rm L}$, respectively.

The LOS of PPV data is the z-axis for the face-on case, and y-axis for the edge-on case. The chosen resolutions will return clouds with fully and barely resolved properties respectively if the simulated clouds have properties similar to the Galactic GMCs. Velocity resolutions are chosen so that the smallest clouds in both spatial resolutions can span across 2 – 3 velocity channels if following the Larson's relation (cf.,§4.3).

The high-resolution PPV data are created from the high-resolution (1.5 pc) simulation. The pixel size matches to cell size at 1.5 pc. When identifying GMCs in the PPV dataset, we assume the galaxy is observed in ^{12}CO (1–0) (115.2 GHz), the most commonly used transition for GMC observations. Therefore, only cells with a density greater than 100 cm^{-3} were included in the data, corresponding to the excitation density of ^{12}CO (1–0). This is consistent with the cloud identification of the PPP clouds, which selected using a continuous contour at a density of 100 cm^{-3}. The cloud identification algorithm of PPV expects the data to be emission intensity, rather than the gas density followed by simulations. We use a Galactic CO-to-H_2 conversion factor ($X_{\rm CO}$) of 2×10^{20} cm^{-2} (K km s^{-1})$^{-1}$ (Bolatto et al. 2013) to convert between the two. Since we do not consider chemistry nor radiative transfer and the excitation of molecular lines, the conversion factor cancels when we derive the cloud mass, so its precise value does not affect our results. This also means that we have a more accurate mass measurement than real observations, and this work is thus an assessment purely for the unavoidable effects of projection, resolution, sensitivity and cloud identification method in observations, i.e., any discrepancy between the datasets can be largely attributed to these effects. The high-resolution face-on and edge-on PPV data are referred as PPV$^{\rm H}_{\rm face}$ and PPV$^{\rm H}_{\rm edge}$, respectively. Comparisons between PPP$^{\rm H}$ and PPV$^{\rm H}_{\rm face}$ have been presented in Pan et al. (2015).

In observations, the image is formed by convolving the intrinsic structures of the observed target with a two-dimensional Gaussian "beam". The convolution plays a critical role in determining the appearance of the GMCs when the beam size is ≥ GMC size. To reproduce the convolution in the low resolution PPV, the Common Astronomy Software Applications (CASA) package (McMullin et al. 2007) is used to simulate ALMA Cycle 3 (2015 October – 2016 September) ^{12}CO (1–0) observations. The input sky model is the noise-free PPV$^{\rm H}_{\rm edge}$ and PPV$^{\rm H}_{\rm face}$ in unit of flux corrected by the $X_{\rm CO}$, assuming a distance and coordinate of M83. Therefore, all of PPV datasets are created from the simulation with 1.5 pc resolution. CASA task *simobserve* is used to construct the *uv* visibilities for the specified antenna configuration, then *simanalyze* is used to Fourier transform the *uv* visibilities into the image plane. Hexagonal mosaic is adopted for mapping. The observing time of 12-m array is about 1 minute on each mosaic pointing. The baselines range from 14.7 to 538.9 meters. Note that we only use the 12-m array, and the effect of interferometric observation, e.g., short-spacing problem, is kept as part of the comparison because most of extragalactic observations did not have corresponding single dish observation to combine. Around 60% of the total flux (estimated from the noise-free PPV$^{\rm H}$) are

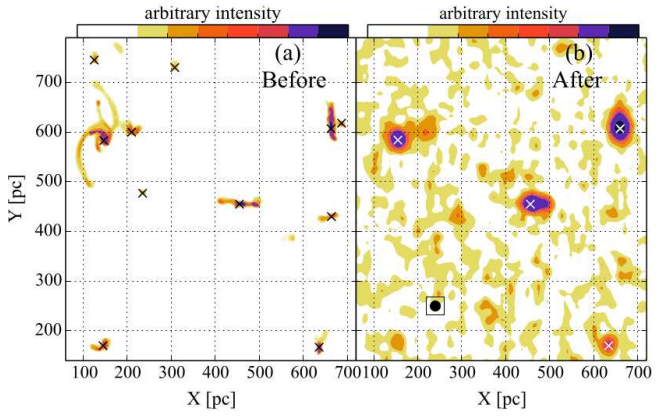

Figure 1. An example of how the ALMA processing affects the data. Panel (a) and (b) show a ~ 700 pc area of the face-on galaxy observed with high and low resolutions (PPV^{H}_{face} and PPV^{L}_{face}), respectively. Beam size (~ 24 pc) of low resolution is shown in panel (b) with solid black circle. Centre of mass of GMCs are marked with black or white crosses. It is clear that because of the low resolution or/and sensitivity in our setup, the small clouds in the high-resolution data disappear in the low-resolution data. Moreover, clouds become more spherical in panel (b) due to the image convolution with the circular beam.

missed. The observation is only sensitive to structures < 500 pc, but is large enough to detect the GMC-scale structures. The final resolution of the low resolution PPV (PPV^{L}_{edge} and PPV^{L}_{face}) are ~ 24 pc (~ 1.3″) and 2 km s^{-1}. The RMS noise level (σ_{RMS}) is ~ 10 mJy (~ 0.55 K), leading to a typical mass sensitivity (1 σ_{RMS} in 1 channel) of 2×10^3 $M_\odot$.

This observation setup is comparable to several ongoing ALMA projects on nearby galaxies. In Figure 1, we present a side-by-side showcase of how the ALMA processing affects the data. Panel (a) and (b) show a ~ 700 pc area seen in PPV^{H}_{face} and PPV^{L}_{face}, respectively. Comparison of two figures show that small clouds in the high-resolution data disappear in the low-resolution data because of the lower resolution or/and sensitivity. Moreover, clouds become more spherical in panel (b) due to the image convolution with the circular beam.

3 DEFINITION OF CLOUDS IN SIMULATION AND OBSERVATION

The cloud identification methods are identical to Pan et al. (2015). In both data structures, GMCs are identified as continuous structures of gas above a chosen density or flux threshold, and multiple peaks are allowed within a GMC. This method, which we refer to as the *island* method in Pan et al. (2015), is the better choice for selecting similar objects between simulation and observation data structures, compared to the *decomposition* method which further segregates the peaks within an island into individual clouds.

PPP works from the lowest density, drawing a contour at $n_{HI,thresh}$ = 100 cm^{-3} and defining all cells within a closed section as the cloud (Fujimoto et al. 2014). PPV clouds are identified using CPROPS (Rosolowsky & Leroy 2006). The package was designed to identify continuous structures in the observed spectral data cube. CPROPS begins by masking the emission with a high signal-to-noise ratio (S/N; 4 × RMS noise in this work), picking out the cloud locations at densities much higher than the background. It then extends this mask to the user defined lowest S/N (2 × RMS noise in this work), which outlines the observed cloud boundary. CPROPS then assumes that the real cloud boundary is larger than the observed cloud boundary, since the cloud outer regions are being obscured by the background noise. It therefore extrapolates linearly from the observed boundary to a sensitivity of 0 K to form the real cloud boundary.

Physical properties of the clouds are derived once the cloud boundaries are set. Derivations of physical properties in PPP and PPV have been fully described in Fujimoto et al. (2014) and Rosolowsky & Leroy (2006), respectively. In this section, we provide a brief qualitative summary. These derivations are not identical between the two methods, since the raw data measure different quantities in different data structures. We do not correct for this, but adopt the original calculations as part of the comparison.

In both data structures, cloud mass is a direct measured property from the sum of cells or pixels enclosed within the cloud boundary. Radius and velocity dispersion of PPP clouds are calculated from three spatial and three velocity dimensions. For cloud radius, the average radius of the cloud is measured from its projected area in the $x-y$, $x-z$, and $y-z$ planes. The mass-weighted one-dimensional velocity dispersion of PPP clouds is computed from the average deviations between the gas velocity and the cloud bulk velocity in x, y, and z direction. PPV, however, must measure the mass(flux)-weighted projected radius at the plane perpendicular to the LOS (note that PPP does not consider any weighting in deriving radius) and the mass(flux)-weighted velocity dispersion along the LOS using the second moments of the emission along the spatial and spectral axes.

The derived cloud properties, that depend on multiple cloud variables, are calculated from the three basic properties above. Surface density, Σ_c, is defined as the mass per unit area and is simply calculated from the cloud mass and radius. Virial parameter, α_{vir}, measures the gravitational binding of a GMC, assuming a spherical profile and no magnetic support or pressure confinement. The classic derivation is defined as the ratio of virial mass (M_{vir}) to cloud mass (M_c) as $\alpha_{vir} \approx M_{vir}/M_c$, where M_{vir} is calculated from the cloud radius (R_c) and velocity dispersion (σ_c) as $M_{vir} \approx 1040\, R_c\, \sigma_c^2$. $\alpha_{vir} > 2$ indicates that the cloud is gravitationally unbound while $\alpha_{vir} < 2$ are bound clouds (Bertoldi & McKee 1992).

4 RESULTS

4.1 Physical Properties of the GMCs in the High Resolution Analysis

The probability distribution function of the high-resolution cloud properties are shown in the upper panel of Figure 2b – 2f. Green-solid, red-dashed , and blue-dotted curves represent PPP^{H}, PPV^{H}_{edge} and PPV^{H}_{face}, respectively. The coloured vertical lines indicate the median value of the properties for each dataset.

The median value of the cloud mass is consistent between the three datasets at ~ 3×10^5 $M_\odot$, but shapes of the profiles slightly differ. PPP^{H} and PPV^{H}_{face} have almost identical mass profile. Pan et al. (2015) found that as high as 70%

Table 1. Summary of the datasets in this work.

	3D clouds		edge-on observations		face-on observations	
	PPP^H	PPP^L	PPV^H_{edge}	PPV^L_{edge}	PPV^H_{face}	PPV^L_{face}
Dataset final resolution [pc]	1.5	24	1.5[a]	~ 24[b].	1.5	~ 24
Resolution of simulation [pc]	1.5	24	1.5	1.5	1.5	1.5
PPV convolved by CASA	...	...	N	Y	N	Y
Representation of resolution	AMR level of simulation	AMR level of simulation	pixel size (MW- and LG-like obs.[c])	beamsize from CASA (extragalactic obs.)	pixel size (MW- and LG-like obs.)	beamsize from CASA (extragalactic obs.)
Note	Pan et al. (2015)[d]	...	...	assume ALMA obs.[e]	Pan et al. (2015)	assume ALMA obs.

[a] We use PPV^H to denote "PPV^H_{edge} and PPV^H_{face}".
[b] We use PPV^L to denote "PPV^L_{edge} and PPV^L_{face}"
[c] MW: Milky Way; LG: Local Group
[d] Detailed comparison of PPP^H and PPV^H_{face} are shown in Pan et al. (2015).
[e] CASA can generate the visibilities measured with ALMA, VLA, CARMA, SMA, and PdBI. ALMA is chosen for this work.

of clouds have single counterpart in both data structures with a mass difference of < 50%.

The blending effect is evident for PPV^H_{edge} as demonstrated in Figure 3(a). The figure shows the galactocentric distribution of cloud numbers. Line styles and colors are the same as in the 1D profiles. Galactocentric distance (R_g) of PPP^H and PPV^H_{face} are calculated by their 3D and 2D position, respectively. PPV^H_{edge}, however, must use the kinematic distance. If LOS velocities are known, clouds at a particular velocity can be assigned a position along the LOS, and thus a particular R_g. The method introduced by Yim et al. (2011) is adopted for this. All three data structures detect two concentrations of clouds at radii $R_g \approx 2-3$ kpc and $R_g \approx 6-7$ kpc, corresponding to the radii of the galactic bar and the spiral arms. However, the number of clouds in PPV^H_{edge} lies below both the PPP^H and PPV^H_{face} cases by ~ 2 times, indicating the cloud blending. Therefore, even though the range and profile of the cloud mass in PPV^H_{edge} do not deviate significantly from that of PPP^H and PPV^H_{face} overall, this should not lead to the interpretation that the cloud mass between the three data sets are the same.

The cloud radii identified in PPV^H_{edge} are smaller compared to the other two datasets (Figure 2c). This is due to the flat galactic disc (Figure 2a), and is visualized in Figure 4. Figure 4(a), (b) show the slice plots of a 400 pc patch of PPV^H_{face} and PPV^H_{edge}, respectively, and the corresponding projection plots in panel (c) and (d). Only the cells with density > 100 cm^{-3} are plotted, therefore most of the coloured regions have been assigned to clouds. It can be seen from panel (b) that clouds are flat in the z-axis, and consequently, the slice and projection plots of PPV^H_{face} (panel (a) and (c)) show higher similarity and less crowding due to the small depth of the LOS, and vice versa for panel (b) and (d). The gas scaleheight of our simulated galaxy is about 80 -âĂŞ 115 pc, which is similar to the initial value of 100 pc due to the lack of stellar feedback to inject energy; nevertheless, recent observations of edge-on spiral galaxies show that the scaleheights of molecular gas traced by ^{12}CO (1-âĂŞ0) are mostly < 150 pc (Yim et al. 2011, 2014), so this effect replicates true observations as well. The velocity dispersion shows very little difference between PPV_{edge} and PPP^H/PPV^H_{face} (Figure 2d). All of methods suggest a median value of ~ 5 km s^{-1}.

In the analysis of this simulation using the same cloud identification method, Fujimoto et al. (2014) found that PPP^H clouds fall into three populations: the most common 'Type A' clouds, with properties that corresponded to the average values measured in observations, the 'Type B' massive giant molecular cloud associations that formed during repeated mergers of smaller clouds, and the transient 'Type C' that were born in tidal tails and filaments. The three types result in the bimodal distribution of cloud surface density (Σ_c) at ~ 1000 $M_\odot$ pc^{-2} ('Type A' and 'Type B') and ~ 100 $M_\odot$ pc^{-2} ('Type C') as seen in the Σ_c profile of PPP^H (Figure 2e).

The clouds in the PPV^H_{face} data also split into two Σ_c regimes, as seen in Figure 2e, but the gap is not as sharp as in PPP^H. Fractions of each cloud type in the entire galaxy differ by less than 10% between PPP^H and PPV^H_{face} (Pan et al. 2015). Moreover, among the clouds that have a direct match in both datasets, ~ 80% are categorized as same type between these two data structures. On the contrary, the bimodal Σ_c is barely seen in PPV^H_{edge}, presumably due to the decrease of cloud radius and cloud blending that increases Σ_c. For the former effect, we would expect an increase of Σ_c for all GMCs, but it is not the case for the high-Σ_c population since the peak of its 1D profile is close to other two datasets. Therefore, the cloud blending is likely in charge of the missing bimodal-Σ_c in PPV^H_{edge}, with the small transient populations most susceptible to blending.

The median value of $\alpha_{vir} \approx 1$ indicates that the majority of the clouds are bound in all three datasets. The main difference is the extension of the profiles to lower values of α_{vir} in two PPV^H sets. The discrepancy arises because of the underestimation of cloud velocity dispersion in PPV^H_{face} and cloud radius in PPV^H_{edge} when the LOS goes along the short and long dimension of the clouds, respectively. .

4.2 Effect of Resolution

In this section, we compare the low-resolution cloud properties between PPP^L, PPV^L. We emphasize again that the low-resolution PPP and PPV clouds are identified from different simulations (§1 and Table 1) due to the different origin of "resolution". In simulations, resolution is set by the

AMR level, which locally refines the mesh to where they are needed. On the other hand, resolution is determined by the size of the beam that is used for convolving an object with finite (high) resolution in observation.

4.2.1 PPP Clouds: Effect of Resolution (Cloud Blending)

We start with the result of the PPP clouds, since it illustrates the blending effect without any influence of the cataloging algorithms. In other words, it represents the best possible case, though it is observationally infeasible.

The property and galactocentric profiles are shown in the lower panels of Figure 2b – 2f and Figure 3(b). Line styles and colors are the same as in the high-resolution plots.

The number of $\mathrm{PPP^L}$ clouds is smaller than that of $\mathrm{PPP^H}$. This is a result of fewer refinement levels. In spite of the different cloud numbers, both resolutions show an accumulations of clouds at the bar ($R_\mathrm{g} \approx 3$ kpc) and spiral ($R_\mathrm{g} \approx 6 - 8$ kpc) regions in Figure 3(b). This suggests that although the blending effect may alter cloud properties, simulations can potentially see the spatial distribution of clouds regardless of resolution.

For the cloud mass distribution in Figure 2b, the range of the profiles are comparable between $\mathrm{PPP^H}$ and $\mathrm{PPP^L}$, but $\mathrm{PPP^L}$ sees more massive clouds at $\sim 10^7$ $\mathrm{M_\odot}$ and fewer small clouds at $< 2 \times 10^5$ $\mathrm{M_\odot}$ as a result of cloud blending. The median mass then increases by ~ 5 times from $\mathrm{PPP^H}$ to $\mathrm{PPP^L}$.

The median cloud radius (Figure 2c) also increases to ~ 40 pc in $\mathrm{PPP^L}$. This is because the cells in the low resolution simulation are larger, so clouds blend to become extended structures. Resolution does not affect the velocity dispersion significantly in Figure 2c, where the range and profile of the distributions are similar between $\mathrm{PPP^L}$ and $\mathrm{PPP^H}$.

Σ_c, the surface density, is significantly affected by resolution. The lower resolution simulation blurs the distinction between the three cloud types as seen in Figure 2e. $\mathrm{PPP^L}$ show a uniform Σ_c at ~ 200 $\mathrm{M_\odot\ pc^{-2}}$. This is in agreement with lower resolution studies performed by Tasker & Tan (2009). The bimodal Σ_c no longer exists in $\mathrm{PPP^L}$, suggesting that the clouds formed via different mechanisms (the three types cloud) cannot be differentiated at 24 pc resolution, even though the cloud properties are extracted directly from 3 dimensions.

The distribution of α_vir suggests that the majority of $\mathrm{PPP^L}$ clouds are gravitationally bound as in $\mathrm{PPP^H}$. The profile of the distribution is also in good agreement between two resolutions. Therefore, resolution may not be a worrying issue for the dynamical state of PPP clouds.

4.2.2 PPV Clouds: The Combination of Resolution (Blending), Sensitivity and Projection Effects in Observer Space

In addition to the resolution or blending effect, casting into observer space invokes sensitivity and projection effects as well. Here we compare the results between $\mathrm{PPV^L_{face}}$ and $\mathrm{PPV^L_{edge}}$, as well as their high-resolution counterparts and PPP clouds.

As seen in the high resolution data in Figure 3(a), the cloud number in the $\mathrm{PPV^L_{edge}}$ is smaller by a factor of $\sim 1.5 - 2$ compared to $\mathrm{PPV^L_{face}}$, except for the central 1 kpc area. Moreover, it is notable that the galactocentric distribution of the $\mathrm{PPV^L_{edge}}$ dataset decreases with radius, while $\mathrm{PPV^L_{face}}$ still observe two crowded regions around the galactic bar and spiral arms at $R_\mathrm{g} \approx 2 - 3$ and $6 - 8$ kpc as seen in $\mathrm{PPP^L}$, but the cloud numbers are not the same. This implies that with low but realistic resolution, edge-on observation no longer sees the real distribution of clouds, and the comparison between face-on observation ($\mathrm{PPV^L_{face}}$) and simulation ($\mathrm{PPP^L}$) should be carried out with great care as well.

The median values of cloud mass in Figure 2b are consistent among $\mathrm{PPV^L_{face}}$, $\mathrm{PPV^L_{edge}}$, and $\mathrm{PPP^L}$ within a factor of 2, but the profile shapes are different. The mass of the $\mathrm{PPV^L_{edge}}$ clouds are slightly larger than $\mathrm{PPV^L_{face}}$. $\mathrm{PPP^L}$ shows a wider range in mass compared to $\mathrm{PPV^L}$ at both ends. At the higher end, the massive $\mathrm{PPP^L}$ clouds are the result of cloud blending as mentioned above. This can be seen in the cloud radius shown in Figure 2c as well (note that this is not exactly the same as convolving the high-resolution simulation to low resolution for making $\mathrm{PPV^L}$). For the lower end, our observational setups of $\mathrm{PPV^L}$ can only extract properties from the clouds with mass $\geq 5 \times 10^4$ $\mathrm{M_\odot}$, leading to the absence of small clouds. If these data were observed with a perfect instrument to a lower noise level or higher sensitivity (but the same resolution of ~ 24 pc), e.g., naively increase the integration time by 100 times, we would then be able to see more small clouds, but most of them do not survive the spatial and/or velocity deconvolution in CPROPS. Therefore, to obtain the small clouds (the Type C clouds), both high resolution and high sensitivity are needed.

A caution that arises from this comparison is that the difference in the median mass among $\mathrm{PPV^L_{face}}$, $\mathrm{PPV^L_{edge}}$, and $\mathrm{PPP^L}$ are unlikely to be found in real observations. The differences are comparable to the uncertainty of X_CO derived from various methods (Bolatto et al. 2013, and reference therein), i.e., projection effects can be obscured by adopting a different X_CO. We should bear in mind this essential point when comparing GMC properties between galaxies.

The median cloud radius becomes ~ 30 pc in $\mathrm{PPV^L}$ as we progress to lower resolution. The large median value compared to the high-resolution counterpart is mostly due to the cloud blending, but note that small clouds also disappear due to insufficient sensitivity or resolution that pushes the median value toward larger end. The median radius of $\mathrm{PPV^L}$ is slightly smaller than $\mathrm{PPV^H}$. In addition to the blending effect from the mesh refinement, the large value of $\mathrm{PPP^L}$ is due in part to the derivation of cloud radius. We did not attempt to correct the resolution effect (e.g., deconvolution) in $\mathrm{PPP^L}$, but keep the same derivation as our previous studies (Fujimoto et al. 2014; Pan et al. 2015), while CPROPS performs spatial deconvolution on cloud radius. The median velocity dispersion of $\mathrm{PPV^L_{edge}}$ clouds increases to ~ 10 km $\mathrm{s^{-1}}$, while it is $5 - 6$ km $\mathrm{s^{-1}}$ in $\mathrm{PPV^L_{face}}$ (Figure 2d), comparable to $\mathrm{PPP^L}$. It is the low resolution and blending effect cause the LOS to pass through a considerably longer path within the $\mathrm{PPV^L_{edge}}$ clouds than for the other two datasets that increases the velocity dispersion significantly.

Both $\mathrm{PPV^L_{face}}$ and $\mathrm{PPV^L_{edge}}$ show a more uniform Σ_c (Figure 2e) as seen in $\mathrm{PPP^L}$. The median values of Σ_c is ~ 200 $\mathrm{M_\odot\ pc^{-2}}$ for $\mathrm{PPV^L_{face}}$, which is again in good agreement with $\mathrm{PPP^L}$, while the value is about two times higher for $\mathrm{PPV^L_{edge}}$.

Both values are very similar to that of the observed "classic" GMCs in the Milky Way and nearby galaxies. Therefore we cannot rule out the possibility that the constancy of the observed Σ_c is due to low resolution. Resolution has a smaller effect on α_{vir} for PPV^L_{face} (Figure 2f). The majority of clouds are gravitaionally bound with median α_{vir} of 1 – 2 as suggested by PPP^L, but note that the range is wider in PPV^L_{face}. In contrast, median α_{vir} of PPV^L_{edge} increases to ~ 4 mostly because velocity dispersion is squared to calculate α_{vir}, leading to an opposite implication that overall the clouds are not bound.

4.3 The Larson's Scaling Relations

The physical properties of GMCs are believed to regulate star formation. This was first observed by Larson (1981) using the Galactic GMCs. He found that GMCs are characterized by M_c-R_c and σ_c-R_c scaling relations as:

$$M_c \propto {R_c}^a,\ \sigma_c \propto {R_c}^b. \quad (1)$$

The relations and the power-law index a and b have been interpreted as evidence that GMCs are supported by internal turbulence, have constant Σ_c and are gravitationally bound. To date, Larson's scaling relations have been tested across different galaxy environments and used to interpret whether GMC properties are universal (Oka et al. 1998; Heyer et al. 2009; Hughes et al. 2010; Rebolledo et al. 2012; Colombo et al. 2014; Rebolledo et al. 2015; Swinbank et al. 2015; Utomo et al. 2015; Leroy et al. 2015). However, no solid conclusion has been reached yet. Theoretical studies also attempt to explain the Larson's relations using numerical simulations (Vázquez-Semadeni et al. 1997; Ostriker et al. 2001; Ossenkopf & Mac Low 2002; Ballesteros-Paredes et al. 2011; Kritsuk et al. 2013; Fujimoto et al. 2014; Ward et al. 2015). They found that the constant Σ_c of GMCs may be the result of saturation of the emission, an optically thick effect, or the limited dynamical range in density available in which the particular tracer can be excited. (Kegel 1989; Ossenkopf et al. 2001; Ballesteros-Paredes & Mac Low 2002; Ballesteros-Paredes 2006). In addition, Shetty et al. (2010) show that the power-law indices of the scaling relations vary between PPP and PPV clumps within a simulated GMC. The discrepancy arises from the projection effect and the difficulty in measuring properties of non-spherical clumps from observations. If this is really the case, then the effects may be more significant for GMCs since they are presumably more structured with multiple clumps, cores and envelopes than the small interior clumps.

Figure 5a and 5b show the Larson's relations for the high- and low-resolution clouds respectively. From the top to bottom rows, we present the relations for M_c-R_c, σ_c-R_c, and α_{vir}-R_c. The left to right columns present the results of PPP, PPV_{edge}, and PPV_{face}, respectively. The fit is performed using the `POLYFIT` function of `Python`'s `NumPy` package. `POLYFIT` can be used to fit a polynomial of specified order to data using a least-squares approach. The 1-σ uncertainty is estimated from the covariance matrix of the fit. The power-law index and the uncertainty of the first two relations are shown in each panels. The dotted lines in M_c-R_c relations denote Σ_c = 50 (lower), 230, 1000, and 5000 (upper) $M_\odot$ pc^{-2}, respectively.

4.3.1 Mass–Radius Relation

In all cases, M_c-R_c relation shows a strong correlation. In the high-resolution clouds, the best-fit line gives a power-law index $a \approx 3.6$ for PPP^H. This is a result of the bimodal-Σ_c, for which both sequences have gradient of 3. $a \approx 3$ for 3D clouds indicates that the GMCs have constant volume densities. The same index is found for the PPP clumps of Shetty et al. (2010). For PPV^H_{edge} and PPV^H_{face}, the best-fit indices with all clouds are $a \approx 3.0$ and 2.5, respectively.

Observations of the edge-on Milky Way normally found a value of $2.0 < a < 3.0$ (e.g., Solomon et al. 1987; Simon et al. 2001; Roman-Duval et al. 2010), our value is located in the higher end. Face-on observations of nearby galaxies have not achieved such high resolution. Observations of the relatively face-on (barred) spiral galaxies LMC and M33 yielded an index a of 2.23 ± 0.08 and 1.89 ± 0.16 with an observed resolution lower than our PPV^H_{face} data but higher than PPV^L_{face} (Rosolowsky et al. 2003; Wong et al. 2011). The index of PPV^H_{face} is comparible to the simulated PPV clumps of Shetty et al. (2010), where they also took a projection along the z-axis.

The discrepancy between PPV^H_{edge} and PPV^H_{face} originates from the different slopes of their low-Σ_c clouds (< 230 $M_\odot$ pc^{-2}) that form in tidal tails and filaments, with a = 3.19 ± 0.13 for PPV^H_{edge} and a = 2.44 ± 0.06 for PPV^H_{face}. This is because it is more difficult to fully identify the cloud boundary of small clouds in PPV space (Shetty et al. 2010; Pan et al. 2015). Moreover, some of the low-mass PPV^H clouds are part of larger PPP^H clouds. PPP^H cloud can be split due to internal motions or the projected density of substructures below the noise level. Finally, the steep a of the low-Σ_c PPV^H_{edge} clouds is also attributed to the rapid growth in cloud mass by the blending and projection effect with respect to the confined cloud radius due to the flat disc.

For the high-Σ_c clouds (> 230 $M_\odot$ pc^{-2}), PPV^H_{edge} and PPV^H_{face} show similar slopes, with a = 2.00 ± 0.07 and a = 2.15 ± 0.10, respectively, implying that structures with larger mass are more likely to have constant column densities. However, this has to be considered with caution because there are a few factors that might have caused the uniform Σ_c. The mass (flux) contrast between the core(s) and envelope of a PPV^H_{edge} cloud may be reduced when the extended envelope are projected along a specific LOS that increases the observed Σ_c, leading to a relatively uniform Σ_c on the surface of the cloud. The aforementioned mass weighting causes PPV^H_{face} cloud radii to be dominated by the high-density (mass) cores, therefore the M_c-R_c relation is dominated by particular regions (Pan et al. 2015). This effect would be reduced to some extent in real observations since the dense regions are consumed to form stars when the density is sufficiently high. This means that the difference between a of PPV^H_{edge} and PPV^H_{face} would enlarge because the relation of PPV^H_{face} would become shallower. Taking account of these, we cannot conclude that the column density of the high-Σ_c clouds is equivalent everywhere in these synthetic observations.

Moving to the low-resolution clouds in Figure 5b, power-law indices a decrease strongly when the resolution is lowered. This is true for all data structures. The power-law index of PPP^L, PPV^L_{edge}, and PPV^L_{face} decreases to $a \approx$ 3.4, 1.3, and 0.6, respectively. The reason for the decreasing

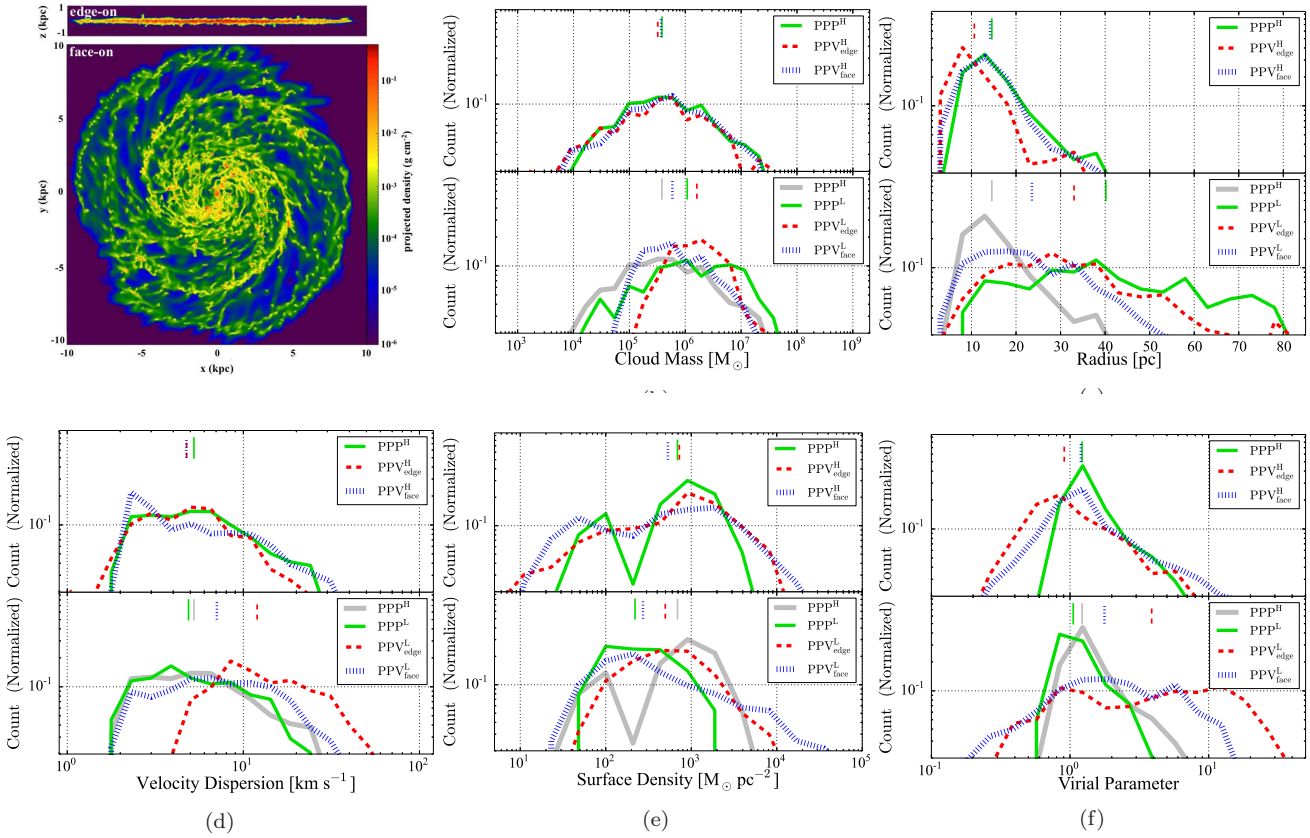

Figure 2. (a) Edge-on (top) and face-on (bottom) projection images of the simulated galaxy in high resolution. (b) Normalized distribution of cloud mass in high (top) and low (bottom) resolutions. Green-solid, red-dashed, and blue-dotted curves denote the distribution of PPP, PPV_{edge}, and PPV_{face}, respectively. In the bottom plots, we overlay the distribution of high-resolution PPP clouds (the green curves in the upper panels) to compare since it represents the "real" case. The coloured vertical lines denote the median value of each parameter. (c) Radius. (d) Velocity dispersion. (e) Surface density. (f) Virial parameter with the same segregation for both resolutions.

a is that the resolution has a notable effect on the cloud surface density, where the high-Σ_c population is missing due to the increase in radius, pushing their relation to low-Σ_c for a given mass. It is worth noting that the order of the three slopes is not changed as we progress to lower resolution. In PPV^{L}_{face}, there is an outlier group of relatively massive clouds sitting at mass $\geq 10^6$ $M_\odot$ but with radii of ≤ 20 pc. The radii of these massive non-star-forming clouds are likely underestimated due to the high density cores taking over the weighting. These clouds occupy about 10% of total populations. Even excluding these clouds arbitrarily, M_c-R_c relation of PPV^{L}_{face} is still flatter than that of PPV^{L}_{edge}.

Low-resolution observations of nearby galaxies obtain an index a in the range of $\sim$ 1.5 – 2.6 (Engargiola et al. 2003; Bolatto et al. 2008; Rebolledo et al. 2012; Donovan Meyer et al. 2013; Colombo et al. 2014; Utomo et al. 2015). The values are larger than our derived values for both PPV^{H}. In observations, M_c is usually calculated by adopting a constant X_{CO} for all clouds, or represented by the measured CO luminosity (L_{CO}). However, there is growing evidence that X_{CO} is not constant among GMCs. Small clouds which have higher fraction of CO-dark molecular gas require larger X_{CO} to recover the H_2 mass from L_{CO}. Thus we would expect that the observed M_c-R_c of nearby galaxies would become shallower once the variable X_{CO} is considered.

4.3.2 Velocity Dispersion–Radius Relation

Results of σ_c-R_c are shown in the middle panels of Figure 5. The best fits of all clouds produce a gradient of $b \approx 1.2$ for PPP^{H} and $b \approx 1.0$ for PPP^{L}. Variation of σ_c-R_c relation is seen for both resolutions at low (< 4 km s^{-1}) and high (> 4 km s^{-1}) σ_c. We thus also perform the fit only considering those structures separately, yielding a b of 0.50 ± 0.05 and 0.46 ± 0.03 for the low-σ_c clouds in PPP^{H} and PPP^{L}, and b of 1.13 ± 0.02 and 1.05 ± 0.06 for the high-σ_c structures, respectively. The results suggest that resolution has relatively small effect on both Larson's relations when the cloud properties are extracted from 3 dimensional measurements. But note that the high and low-σ_c (or Σ_c) clouds are relatively discrete in the high-resolution relations, while they are continuous in the low-resolution relations due to the removal of the three types populations.

For the PPV clouds, there is a large discrepancy in the σ_c-R_c relation between the four datasets. As seen in

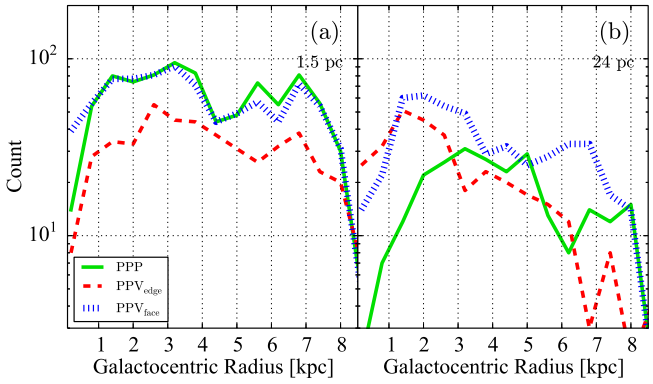

Figure 3. Galactocentric distribution of cloud numbers in (a) high and (b) low resolutions. Green-solid, red-dashed, and blue-dotted curves represent the clouds from PPP, PPV_{edge}, and PPV_{face}, respectively. Galactocentric distance of PPP and PPV_{face} are calculated by 3- and 2-dimensional position, respectively, while PPV_{edge} adopts kinematic distance using the method introduced in Yim et al. (2011). In the high resolution, the cloud numbers are similar across all datasets, showing two concentrations at the radii of galactic bar and spiral arms. However, the cloud number of PPV^{H}_{edge} lies below PPP^{H} and PPV^{H}_{face} by roughly a factor of two, indicating the cloud blending. In the low resolution, PPV^{L}_{edge} no longer represents the intrinsic distribution of clouds, but decline with radius, whereas PPV^{L}_{face} show a similar profile as PPP^{L} and their high-resolution counterparts, but with fewer clouds everywhere.

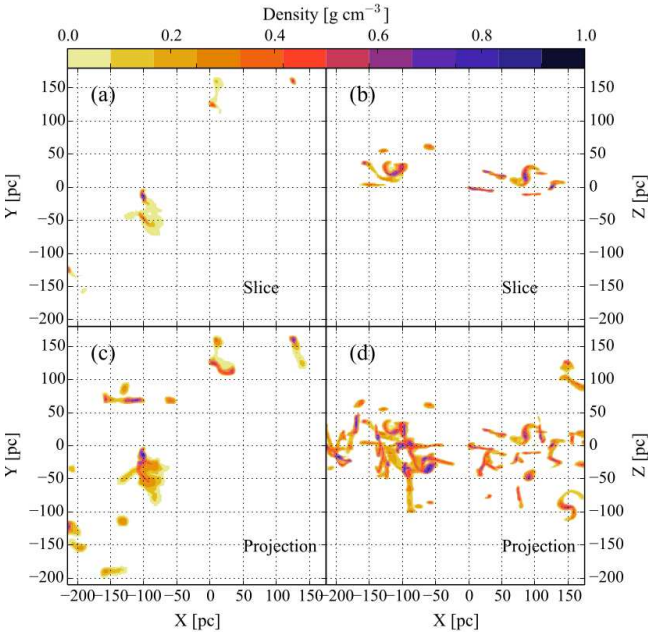

Figure 4. Example of GMCs seen from different viewing angle of *z*-axis (face-on, left) and *y*-axis (edge-on, right). Note that *y*-axis ticks of the edge-on cases (panel b and d) are shown at the right-hand side. Only the cells with density > 100 cm^{-3} are plotted, therefore most of the coloured regions have been assigned to clouds. Panel (a) and (b) present the slice plots of face-on and edge-on views, respectively, panel (c) and (d) show projection plots of the the same orientations.The representative region is located at the spiral arm with galactocentric radius of ~ 6 kpc. It can be seen from panel (b) that clouds are flat in the *z*-axis, and consequently, the slice and projection plots of PPV^{H}_{face} (panel (a) and (c)) show higher similarity and less crowding due to the small depth of the LOS, and vice versa for panel (b) and (d).

the M_c-R_c relation, the best-fitting power law indices flatten from high to low resolution, and from edge-on to face-on observation with $b \approx 0.8$ and 0.5 for PPV^{H}_{edge} and PPV^{H}_{face} and $b \approx 0.4$ and 0.0 for PPV^{L}_{edge} and PPV^{L}_{face}, respectively. Observations also suggest a large range of index between $b \approx 0 - 2$, and there is no obvious correlation between the observed resolution, disc inclination and the derived index (Engargiola et al. 2003; Rosolowsky et al. 2003; Rosolowsky 2007; Bolatto et al. 2008; Wong et al. 2011; Donovan Meyer et al. 2013; Colombo et al. 2014; Rebolledo et al. 2015; Utomo et al. 2015). Interestingly, the weak to no correlations of PPV^{L}_{edge} and PPV^{L}_{face} are in line with the latest unresolved observations of GMCs (Colombo et al. 2014; Rebolledo et al. 2015; Utomo et al. 2015; Leroy et al. 2015).

In fact, it is unlikely that the σ_c-R_c relation would be identical between PPV datasets when both variables are projection-dependent but molecular clouds have non-spherical shapes (e.g., Falgarone et al. 1991; Shetty et al. 2010; Khoperskov et al. 2015). For example, if the LOS goes along the short dimension of the cloud, the use of PPV can result in an overestimation of R_c along with an underestimation of σ_c. This can explain why the high resolution face-on observation suggest large amount of clouds with low σ_c (Figure 2d and 5a).

A notable feature of the power-law indices a and b is the marked difference across low-resolution datasets compared to high resolution. The discrepancy arises maybe because the resolution of ~ 24 pc can randomly sample various combination of cloud (or ISM) structures (see also Calzetti et al. 2012). In other words, the resolution resolves neither the individual GMCs nor the full cloud mass spectrum, which may be used to interpret the composition of GMCs within an area. The measured cloud properties are therefore sensitive to their intrinsic properties and the geometry of cloud distribution, which includes the intrinsic and projected distributions. Hence, the derived cloud properties and the scaling relation with this resolution are not entirely driven by the underlying physical origin.

Our results of two Larson's relations suggest that such scaling relations may not genuinly reflect the physical properties and the dynamical state of GMCs. Therefore, Larson's relations should not be used alone to interpret the physical properties and the environmental dependence of GMCs.

4.3.3 Virial Parameter-Radius Relation

PPP^{H}_{edge} clouds show two populations on the α_{vir}-R_c plane in the bottom row of Figure 5a. The unbound population ($\alpha_{vir} > 2$) sitting at the small R_c regime shows decreasing α_{vir} with R_c, i.e., the smaller clouds are the least gravitationally bound. These are the 'Type C' clouds with $\Sigma_c < 230$ M$_\odot$ pc^{-2}. The bound population with $\alpha_{vir} \approx 1$ spreads out over a wide range of R_c and show α_{vir} increasing with R_c. These are the 'Type A' and 'Type B' with high Σ_c.

The three type clouds and their distinct α_{vir} are reproduced but more scattered in PPV^{H}_{edge} and PPV^{H}_{face} clouds (Pan et al. 2015). Overall, PPV^{H}_{face} clouds share the same features as PPP^{H}. For the PPV^{H}_{edge} clouds, even though the

Type C clouds are not clear on the M_c-R_c relation, it is visible in the α_{vir}-R_c relation. This population has considerably high α_{vir} and show the same variation in R_c as seen in PPP^H and PPV^H_{face}. The bound population of PPV^H_{edge}, however, shows a weak correlation between α_{vir} and R_c. The values are concentrated around 1 from $R_c \approx 5 - 50$ pc, but slightly increase toward $R_c \approx 80$ pc. This is because R_c of PPV^H_{edge} clouds are relatively uniform around 10 pc (Figure 2c) due to the flat galactic disc.

Turning to the low resolution, PPP^L clouds show similar features to PPP^H in the α_{vir}-R_c relation, however, the variation of cloud properties have a very notable effect on α_{vir} for the low-resolution PPV cloud (bottom rows of Figure 5b). α_{vir} for PPV^L_{face} clouds increase with R_c, indicating that the large clouds are least bound. The pattern and the underlying implication are similar to the bound population in its high-resolution counterpart, but the relation is much more scattered. We note that a high-α_{vir} cloud is harder to detect than a lower-α_{vir} cloud with the same M_c because the spread over larger R_c or σ_c will make the surface brightness per channel lower. PPV^L_{edge} clouds show different distribution characteristics, including two concentrations with a dominant population at $\alpha_{vir} \approx 1$ and a secondary at $\alpha_{vir} \approx 3 - 10$. We found that the unbound populations tend to have relatively large σ_c and small M_c. Because α_{vir} is proportional to the square of σ_c and inverse of M_c, α_{vir} then increases significantly. This is in agreement with previous argument that small clouds are more susceptible to (velocity) blending. The blended emission can spread out over a wide velocity channels, but M_c does not increase as fast as σ_c since they are intrinsically small.

The large discrepancy in α_{vir} can lead to inaccurate interpretations of the dynamical state of GMCs, and therefore their potential for star formation (e.g., Ballesteros-Paredes 2006). Shetty et al. (2010) and Beaumont et al. (2013) have also recognized the difficulty to determine α_{vir} in their simulated PPV clumps even though the clumps are more compact with less substructure than our GMCs. Shetty et al. (2010) further suggest that the classic derivation of α_{vir} for simple spherical structures may not be sufficient to reliably determine if a GMC is bound or not. Revision is required to handle the non-spherical shapes and projection effects and to include additional physics in both PPP and PPV clouds, such as Σ_c, magnetic fields, and time (Bertoldi & McKee 1992; Ballesteros-Paredes 2006; Dib et al. 2007; Shetty et al. 2010; Hernandez & Tan 2011). That is, dynamical state of the GMCs may not be single value to be determined.

Moreover, our results suggest that the virial mass (M_{vir})-based analysis of extragalactic X_{CO} should be used with caution. Many studies have used the classically derived M_{vir} (§3) of GMCs to estimate the extragalactic X_{CO} assuming virial equilibrium ($M_{vir} \approx M_c$, e.g., Adler et al. 1992; Israel et al. 2003; Rosolowsky 2007; Bolatto et al. 2008; Hughes et al. 2010; Donovan Meyer et al. 2012; Rebolledo et al. 2012). However, our results show that M_{vir} is projection dependent in the PPV space, and therefore the derived X_{CO} would be affected by the observational bias as well. This is particularly true for the low, but realistic, resolution. The estimation of X_{CO} can be improved by increasing the observed resolution as suggested by the similar α_{vir} between the high-resolution datasets (Figure 2f), however, the required resolution can be rather unrealistic for extragalactic observations even with ALMA, e.g., the 1.5 pc in this work.

The results for α_{vir} also imply a significant role for the cloud definition method and selection criteria (e.g., Issa et al. 1990; Sheth et al. 2008; Shetty et al. 2012; Hughes et al. 2013; Fujimoto et al. 2014; Pan et al. 2015; Colombo et al. 2015). There is no obvious edge to the clouds, which are often thought to be borderline of gravitationally bound. However, the required boundary that truncates the cloud from a continuous ISM can change if the clouds are observed from a different direction, different resolution, and different data structure. We emphasize that our analysis is on the basis of a specific cloud identification method which can potentially identify the same objects with close properties between simulations and observations (Pan et al. 2015). It is not necessarily the most suitable method for other datasets, depending on the data quality and the scientific goal. The major reason for the ambiguity here is the absence of a practical "definition" of a giant molecular cloud.

5 SUMMARY

While ALMA is about to resolve a wide population of GMCs across different galaxy environments, understanding the observational bias is essential for obtaining reliable GMC properties. Observational bias, such as the disc inclination and the observed resolution in this work, is assessable by comparing GMC properties found when using observational identification techniques to those typically used for simulation data. To achieve this, we compared the physical properties of GMCs formed in a simulation of a barred spiral galaxy using both simulation and observational identification methods. The two methods identified clouds in the data using the PPP space typical for simulations and the PPV space used in observations. In each case, two resolutions were considered: one at the maximum resolution of the simulation data (1.5 pc) and another at a more realistic level for observational instruments (24 pc). For the PPV data, the galaxy disc was also considered both face-on and side-on, to explore the result of projection effects. The PPV data cube was assumed to be the product of ^{12}CO (1–0) observations.

The main results for the high-resolution (1.5 pc) cloud properties in PPP^H, PPV^H_{edge} and PPV^H_{face} are as follows:

(i) The galactocentric profile of cloud numbers are similar in all datasets, showing two concentrations at the radii of galactic bar and spiral arms. However, the cloud number in the PPV^H_{edge} analysis lies below the PPP^H and PPV^H_{face} datasets by roughly a factor of two, indicating that the clouds are blending when viewed edge-on in PPV space. Thus, even though the distribution and median values of the high-resolution cloud properties (mass and velocity dispersion) agree with each other, this should not lead to the interpretation that the clouds in PPV^H_{edge} and PPP^H/PPV^H_{face} are completely the same.

(ii) Disc inclination has a notable effect on the cloud radius where the results from the PPV^H_{edge} become smaller than the other two datasets due to the flat galactic disc.

(iii) The bimodal mass surface density distribution of PPP^H clouds as a result of different formation mechanisms suggested in Fujimoto et al. (2014), is reproduced by both the PPV^H_{edge} and PPV^H_{face} methods, although the boundary

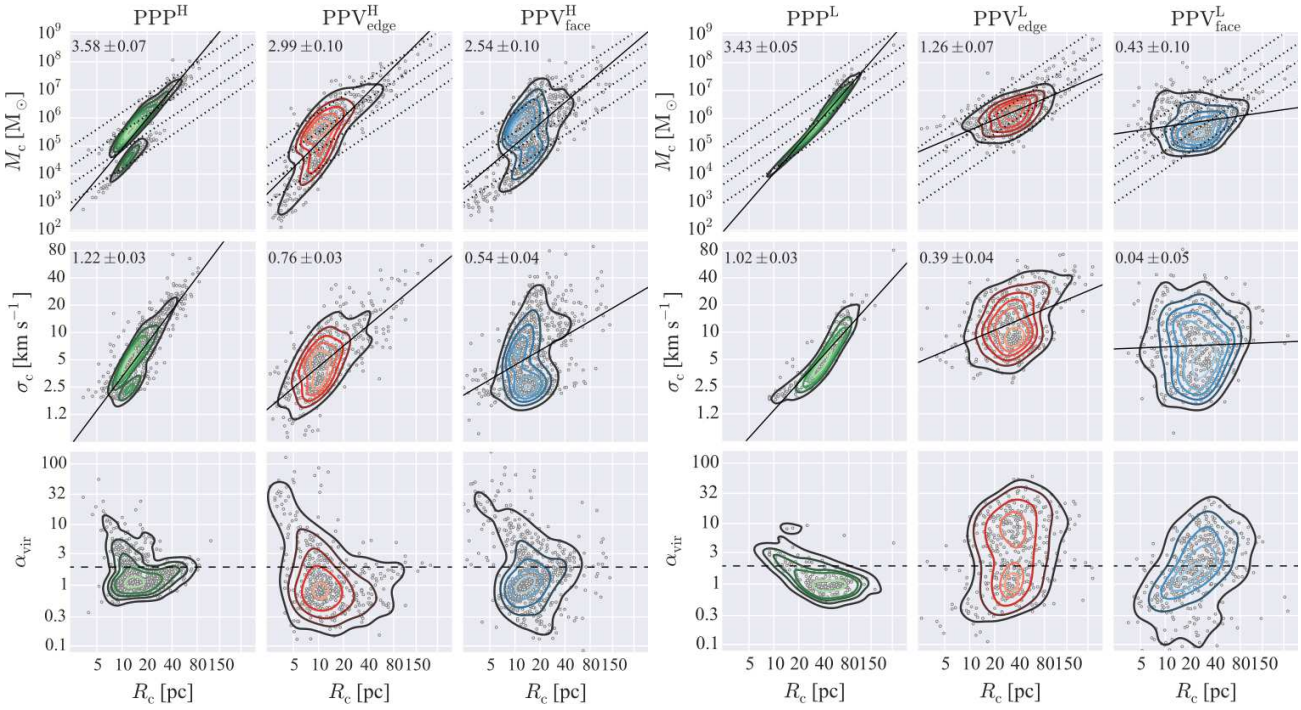

Figure 5. Larson's scaling relations for the identified clouds. From the top to bottom rows, relations for mass-radius ($M_c - R_c$), velocity dispersion-radius ($\sigma_c - R_c$), and virial parameter-radius ($\alpha_c - R_c$) are presented, respectively. The horizontal dashed line in the $\alpha_{vir} - R_c$ relation marks the boundary of virial equilibrium, where $\alpha_c = 2$. The left to right columns show the results of PPP, PPV_{edge}, and PPV_{face}, respectively. Power law index of the first two relations are given in the upper-left corner of the panels. (a) Results with high resolution. Dotted lines denote Σ_c = 50 (lower), 230, 1000, and 5000 (upper) $M_\odot$ pc^{-2}, respectively. (b) Results with low resolution. It is clear that both resolution and inclination effects influence the observed GMC properties and the slopes of Larson's scaling relations.

between the two trends is least distinguishable for PPV^H_{edge}, due to small populations being particularly susceptible to blending.

(iv) The data structure and disc inclination do not significantly affect the virial parameter of the high resolution clouds. All methods determined a median virial parameter of ~ 1.0, suggesting that majority of clouds are gravitationaly bound.

We prepared low-resolution (24 pc) PPV datasets using CASA, allowing us to simulate ALMA observation with realistic resolution and sensitivity (noise level). The low-resolution PPP clouds were identified from a simulation with fewer total levels of refinement. The main results for the low-resolution cloud properties in the PPP^L, PPV^L_{edge} and PPV^L_{face} datasets are:

(i) We first compared the results from PPP^L and PPP^H to evaluate the blending (or resolution) effect alone. This revealed that although the cloud properties change, the simulation can potentially see the spatial distribution and dynamical state of clouds regardless of resolution. However, it is not able to distinguish clouds formed via different formation mechanisms at 24 pc resolution, even though the cloud properties are extracted directly from 3 dimensions.

(ii) When we switched from high to low resolution (and sensitivity) in observations, the smaller clouds are lost. Large clouds are detected but become more spherical than their intrinsic morphology due to the image convolution with the nearly circular beam.

(iii) The galactocentric profile of PPV^L_{edge} no longer represents the intrinsic distribution of clouds, but declines with radius, whereas PPV^L_{face} show a similar profile as PPP^L and their high-resolution counterparts, but with fewer clouds at all radii.

(iv) Overall, we found good agreement between the profiles and median values of the cloud properties between the PPV^L_{face} and PPP^L techniques, while PPV^L_{edge} clouds are more massive and with larger velocity dispersions.

(v) In contrast with the high-resolution data, the mass density is not bimodal in any of the low-resolution data.

(vi) The resolution has an alarming effect on the virial parameter. Median α_{vir} of PPV^L_{edge} suggests that the clouds are not gravitationally bound, which is in contrast to PPP^L and PPV^L_{face}, where the clouds seem to be bound.

We plotted Larson's scaling relations of mass–radius ($M_c \propto {R_c}^a$) and velocity dispersion–radius ($\sigma_c \propto {R_c}^b$) using the measured cloud properties, the main results are:

(i) The power-law indices of the Larson relations change with data structure, disc inclination, and resolution. In all relations, the indices decrease from PPP, PPV_{edge} to PPV_{face} and decrease from high to low resolutions.

(ii) For individual data structures, the power-law index of PPP is relatively insensitive to resolution, while it changes by ≥ 2 times between the two resolutions for both face-on

and edge-on PPV. This suggests that Larson's scaling might be reliable only for the clouds properties extracted from 3 dimensions.

(iii) A discrepancy in the power-law indices between face-on and edge-on observations are also observed. Moreover, the low, but realistic, resolution shows larger discrepancy compared to high resolution. Perhaps because a 24 pc resolution can sample clouds with various combinations, the measured cloud properties and the scaling relations are therefore not representing the true cloud properties.

We also compared the relation between the virial parameter ($\alpha_{\rm vir}$) and $R_{\rm c}$. Results suggest that such scaling relations are not entirely driven by the underlying physical origin of the GMCs. Therefore they should be used with caution when discussing the environmental dependence and the dynamical state of GMCs.

We made a few comments on the CO-to-H_2 conversion factor ($X_{\rm CO}$) in real observations. First of all, the differences in the cloud mass between the low-resolution datasets are comparable to the uncertainty of $X_{\rm CO}$. Thus the observational bias can be obscured by adopting a different $X_{\rm CO}$. Secondly, that a virial mass-based derivation of extragalactic $X_{\rm CO}$ should be used with caution. Our results show that $M_{\rm vir}$ is projection dependent in the PPV space, especially with the low but realistic resolution (24 pc). Therefore the derived $X_{\rm CO}$ would be affected by the observational bias as well. The estimation of $X_{\rm CO}$ can be improved by increasing the observed resolution. However, the required resolution can be rather unrealistic for extragalactic observations even with ALMA, e.g., the 1.5 pc in this work.

Finally we note that this work is based on a specific setup for a simulated galaxy. Observational bias would alter the GMC properties and Larson's relations in different ways if the galaxy type is changed, such as the global morphology and gas content, because they determine the intrinsic distribution and properties of the GMCs.

ACKNOWLEDGMENTS

We thank referee for providing useful comments that have helped to improve the paper. The authors would like to thank the yt development team (Turk et al. 2011) for support during the analysis of these simulations. Numerical computations were carried out on the Cray XT4 and Cray XC30 at the Center for Computational Astrophysics (CfCA) of the National Astronomical Observatory of Japan (NAOJ). EJT is funded by the MEXT grant for the Tenure Track System. SMB acknowledges financial support from the Vanier Canada Graduate Scholarship program.

REFERENCES

Adler, D. S., & Roberts, W. W., Jr. 1992, ApJ, 384, 95
Adler, D. S., Lo, K. Y., Wright, M. C. H., et al. 1992, ApJ, 392, 497
Ballesteros-Paredes, J., & Mac Low, M.-M. 2002, ApJ, 570, 734
Ballesteros-Paredes, J., Hartmann, L. W., Vázquez-Semadeni, E., Heitsch, F., & Zamora-Avilés, M. A. 2011, MNRAS, 411, 65
Ballesteros-Paredes, J. 2006, MNRAS, 372, 443
Beaumont, C. N., Offner, S. S. R., Shetty, R., Glover, S. C. O., & Goodman, A. A. 2013, ApJ, 777, 173
Bertoldi, F., & McKee, C. F. 1992, ApJ, 395, 140
Bertram, E., Shetty, R., Glover, S. C. O., et al. 2014, MNRAS, 440, 465
Bertram, E., Konstandin, L., Shetty, R., Glover, S. C. O., & Klessen, R. S. 2015, MNRAS, 446, 3777
Bolatto, A. D., Leroy, A. K., Rosolowsky, E., Walter, F., & Blitz, L. 2008, ApJ, 686, 948
Bolatto, A. D., Wolfire, M., & Leroy, A. K. 2013, ARA&A, 51, 207
Bryan, G. L., Norman, M. L., O'Shea, B. W., et al. 2014, ApJS, 211, 19
Colombo, D., Hughes, A., Schinnerer, E., et al. 2014, ApJ, 784, 3
Colombo, D., Rosolowsky, E., Ginsburg, A., Duarte-Cabral, A., & Hughes, A. 2015, MNRAS, 454, 2067
Calzetti, D., Liu, G., & Koda, J. 2012, ApJ, 752, 98
Dib, S., Kim, J., Vázquez-Semadeni, E., Burkert, A., & Shadmehri, M. 2007, ApJ, 661, 262
Dobbs, C. L., Burkert, A., & Pringle, J. E. 2011, MNRAS, 417, 1318
Donovan Meyer, J., Koda, J., Momose, R., et al. 2012, ApJ, 744, 42
Donovan Meyer, J., Koda, J., Momose, R., et al. 2013, ApJ, 772, 107
Engargiola, G., Plambeck, R. L., Rosolowsky, E., & Blitz, L. 2003, ApJS, 149, 343
Falgarone, E., Phillips, T. G., & Walker, C. K. 1991, ApJ, 378, 186
Fujimoto, Y., Tasker, E. J., Wakayama, M., & Habe, A. 2014, MNRAS, 439, 936
Hernandez, A. K., & Tan, J. C. 2011, ApJ, 730, 44
Heyer, M., Krawczyk, C., Duval, J., & Jackson, J. M. 2009, ApJ, 699, 1092
Hughes, A., Wong, T., Ott, J., et al. 2010, MNRAS, 406, 2065
Hughes, A., Meidt, S. E., Colombo, D., et al. 2013, ApJ, 779, 46
Israel, F. P., Johansson, L. E. B., Rubio, M., et al. 2003, A&A, 406, 817
Issa, M., MacLaren, I., & Wolfendale, A. W. 1990, ApJ, 352, 132
Kegel, W. H. 1989, A&A, 225, 517
Khoperskov, S. A., Vasiliev, E. O., Ladeyschikov, D. A., Sobolev, A. M., & Khoperskov, A. V. 2015, arXiv:1508.04966
Kritsuk, A. G., Lee, C. T., & Norman, M. L. 2013, MNRAS, 436, 3247
Kruijssen, J. M. D., Longmore, S. N., Elmegreen, B. G., et al. 2014, MNRAS, 440, 3370
Larson, R. B. 1981, MNRAS, 194, 809
Leroy, A. K., Bolatto, A. D., Ostriker, E. C., et al. 2015, ApJ, 801, 25
Longmore, S. N., Bally, J., Testi, L., et al. 2013, MNRAS, 429, 987
McMullin, J. P., Waters, B., Schiebel, D., Young, W., & Golap, K. 2007, Astronomical Data Analysis Software and Systems XVI, 376, 127
Oka, T., Hasegawa, T., Hayashi, M., Handa, T., & Sakamoto, S. 1998, ApJ, 493, 730
Ossenkopf, V., Klessen, R. S., & Heitsch, F. 2001, A&A, 379, 1005
Ossenkopf, V., & Mac Low, M.-M. 2002, A&A, 390, 307
Ostriker, E. C., Stone, J. M., & Gammie, C. F. 2001, ApJ, 546, 980
Pan, H.-A., Fujimoto, Y., Tasker, E. J., et al. 2015, MNRAS, 453, 3082
Pichardo, B., Vázquez-Semadeni, E., Gazol, A., Passot, T., & Ballesteros-Paredes, J. 2000, ApJ, 532, 353
Rebolledo, D., Wong, T., Leroy, A., Koda, J., & Donovan Meyer, J. 2012, ApJ, 757, 155
Rebolledo, D., Wong, T., Xue, R., et al. 2015, ApJ, 808, 99
Roman-Duval, J., Jackson, J. M., Heyer, M., Rathborne, J., & Simon, R. 2010, ApJ, 723, 492

Rosolowsky, E., Engargiola, G., Plambeck, R., & Blitz, L. 2003, ApJ, 599, 258
Rosolowsky, E., & Blitz, L. 2005, ApJ, 623, 826
Rosolowsky, E., & Leroy, A. 2006, PASP, 118, 590
Rosolowsky, E. 2007, ApJ, 654, 240
Sheth, K., Vogel, S. N., Wilson, C. D., & Dame, T. M. 2008, ApJ, 675, 330
Shetty, R., Collins, D. C., Kauffmann, J., et al. 2010, ApJ, 712, 1049
Shetty, R., Beaumont, C. N., Burton, M. G., Kelly, B. C., & Klessen, R. S. 2012, MNRAS, 425, 720
Simon, R., Jackson, J. M., Clemens, D. P., Bania, T. M., & Heyer, M. H. 2001, ApJ, 551, 747
Solomon, P. M., Rivolo, A. R., Barrett, J., & Yahil, A. 1987, ApJ, 319, 730
Swinbank, A. M., Dye, S., Nightingale, J. W., et al. 2015, ApJ, 806, L17
Tasker, E. J., & Tan, J. C. 2009, ApJ, 700, 358
Tasker, E. J. 2011, ApJ, 730, 11
Tasker, E. J., Wadsley, J., & Pudritz, R. 2015, ApJ, 801, 33
Turk, M. J., Smith, B. D., Oishi, J. S., et al. 2011, ApJS, 192, 9
Utomo, D., Blitz, L., Davis, T., et al. 2015, ApJ, 803, 16
Vázquez-Semadeni, E., Ballesteros-Paredes, J., & Rodríguez, L. F. 1997, ApJ, 474, 292
Ward, R. L., Wadsley, J., Sills, A., & Petitclerc, N. 2012, ApJ, 756, 119
Ward, R. L., Benincasa, S. M., Wadsley, J., Sills, A., & Couchman, H. M. P. 2015, arXiv:1510.08187 J. C., & van der Hulst, J. M. 2011, AJ, 141, 48
Wong, T., Hughes, A., Ott, J., et al. 2011, ApJS, 197, 16
Yim, K., Wong, T., Howk, J. C., & van der Hulst, J. M. 2011, AJ, 141, 48
Yim, K., Wong, T., Xue, R., et al. 2014, AJ, 148, 127